Torsional solutions of convection in rotating fluid spheres

J. Sánchez Umbría* and M. Net†
Physics Department, Universitat Politècnica de Catalunya, Jordi Girona Salgado 1–3, Campus Nord, Mòdul B4, 08034 Barcelona, Spain

(Received 8 October 2018; published 25 January 2019)

A numerical study of the nonlinear torsional solutions of convection in rotating, internally heated, self-gravitating fluid spheres is presented. Their dependence on the Rayleigh number has been found for two pairs of Ekman (E) and small Prandtl (Pr) numbers in the region of parameters where, according to Zhang *et al.* [J. Fluid Mech. **813**, R2 (2017)], the linear stability of the conduction state predicts that they can be preferred at the onset of convection. The bifurcation to periodic torsional solutions is supercritical for sufficiently small Pr. They are not rotating waves, unlike the nonaxisymmetric case. Therefore they have been computed by using continuation methods for periodic orbits. Their stability with respect to axisymmetric perturbations and physical characteristics have been analyzed. It was found that the time- and space-averaged equatorially antisymmetric part of the kinetic energy of the stable orbits splits into equal poloidal and toroidal parts, while the symmetric part is much smaller. Direct numerical simulations for $E = 10^{-4}$ at higher Rayleigh numbers (Ra) show that this trend is also valid for the nonperiodic flows and that the mean values of the energies remain almost constant with Ra. However, the modulated oscillations bifurcated from the quasiperiodic torsional solutions reach a high amplitude, compared with that of the periodic, increasing slowly and decaying very fast. This repeated behavior is interpreted as trajectories near heteroclinic chains connecting unstable periodic solutions. The torsional flows give rise to a meridional propagation of the kinetic energy near the outer surface and an axial oscillation of the hot nucleus of the metallic fluid sphere.

DOI: 10.1103/PhysRevFluids.4.013501

I. INTRODUCTION

The thermal convection in rotating self-gravitating fluid spheres and in spherical shells provides simplified mathematical models of the hydrodynamic phenomena taking place in layers or cores of planets and stars. Many approximations are necessary to reduce the problem to one that can be treated by analytical or numerical methods. Usually, the fluids are considered to be pure or with only a few components (see Refs. [1,2], among others). The Boussinesq or the anelastic approximations are used when the compressibility is small. A uniform internal heating is many times assumed, modeling the release of energy by thermonuclear or chemical reactions, or of latent heat due to phase changes, etc. The ellipsoidal shapes are substituted by perfect spheres when the rotation is relatively low, although there are exceptions (see, for instance, Refs. [3,4]). The momentum, energy, and concentration equations can be integrated in time to obtain information from the simulations, or particular invariant objects such as equilibria, waves, or other periodic regimes can be computed with adapted numerical nonlinear solvers. In this latter case it is interesting trying to understand

*juan.j.sanchez@upc.edu
†marta.net@upc.edu

the sequence of transitions from very simple states of the fluid to full developed turbulence. In this article we focus on the fundamental problem of studying the nonlinear properties of the torsional flows generated by internal temperature gradients of a rotating fluid sphere. They can be generated either by thermonuclear reactions, as happens in the massive stars of the main sequence, or by the secular cooling down of a liquid metallic core, as happens, for instance, in Venus or Mars.

In the case of a pure fluid, with the above mentioned approximations, and isothermal nonslip or stress-free boundary conditions, there is a steady state in which the fluid is at rest, and the heat is released through the external boundary by means of internal conduction. The linear theory for the onset of thermal convection in spheres or shells, from this conduction state, has been studied in the past by many authors from several points of view (see Refs. [5–15] among others). The results show that, in general, the solutions after this first transition are symmetric with respect to the equator and are not invariant under rotations with respect to the axis of rotation (nonaxisymmetric). Since the problem depends on several parameters, and their possible ranges of variation are large, there is room for other cases, which can become the preferred situations for particular ranges of the parameters. In the case of shells, it was found that at low Ekman numbers (E) it is possible to find nonaxisymmetric and equatorially antisymmetric modes at the beginning of convection for the very small Prandtl numbers ($\mathrm{Pr} < 0.01$) of the liquid metals [16]. Moreover, preferred torsional modes, i.e., axisymmetric and equatorially antisymmetric modes, were found numerically in rotating fluid spheres for $\mathrm{Pr} \ll 0.01$ at low E [17]. This latter result was confirmed analytically by using asymptotic methods in Ref. [18].

Very recently Kong *et al.* [19] also studied the weakly nonlinear dynamics of the torsional periodic flows of $\mathrm{Pr} = 0.01$ for $\mathrm{E} = 10^{-3}$, by means of time integration in a spherical shell of very small radius ratio $\eta = 0.001$, finding a latitudinal propagation of the patterns of convection, and the loss of stability of the axisymmetric solutions at $\approx 8.2 \times 10^3$ very close to their onset. Their results also show that the bifurcation to torsional flows is supercritical for very low Pr, in agreement with those presented here. They also computed a branch of three-dimensional (3D) azimuthal waves with wave number $m = 1$. However, as the authors mention in their paper, these solutions bifurcate from the conduction state, so nothing is known about the dynamics on the secondary branch of 3D solutions bifurcated from the torsional flows when the invariance by rotation is broken. The dynamics of the 3D solutions will surely be influenced by the dynamics of the axisymmetric flows, even at high Ra. Moreover stable global 3D dynamics in this system can involve the axisymmetric branches of solutions bifurcated from the periodic torsional flows at high Ra. Then it is important to understand the behavior and the route to chaos of the axisymmetric solutions to distinguish their effect on the 3D flows. In fact, the dynamics described by Landeau and Aubert [20], although found for $\mathrm{Pr} = 1$ and a shell of $\eta = 0.01$ with nonslip boundary conditions, could be closely related with the torsional flows reported below. They obtained a transition from the classical columnar convection towards an asymmetric regime, strongly influenced by an axisymmetric, equatorially antisymmetric flow, that was interpreted as the manifestation of the first axisymmetric bifurcation of the conduction state, giving rise to unstable solutions. This study is an example of the importance and influence of the secondary and ulterior bifurcations even if they give rise to unstable flows at the beginning. Although the torsional solutions are not preferred at the onset with nonslip boundary conditions, the linear stability analysis also shows that the torsional modes are present at very low Ra, so it is possible that they give rise to stable solutions at a Rayleigh number not far from the critical.

In a nonlinear problem several stable solutions can coexist, and to obtain one or another depends on the initial conditions. The linear stability analysis of the conduction state for a rotating fluid sphere of $\mathrm{Pr} = 0.01$ and $\mathrm{E} = 10^{-3}$ gives the axisymmetric bifurcation at $\mathrm{Ra}_c = 7.36 \times 10^3$, and that that is 3D with azimuthal wave number $m = 1$ at $\mathrm{Ra} = 7.83 \times 10^3$, so the second branch described by Kong *et al.* [19] bifurcates when the real part of, at least, a second pair of complex eigenvalues becomes positive. Then the 3D branch of waves arising from the conduction state must be unstable. This means that either it is slightly subcritical or it stabilizes very close to the bifurcation point, as happens in the unfolding of a double Hopf bifurcation (see, for instance, Ref. [21]). The closeness

of the critical values given above seems to indicate that the results of Ref. [19] are in agreement with the second scenario.

As said before, the aim of this article is to deepen in the study of the nonlinear dynamics of the torsional flows that arise when a metallic fluid sphere (without any small internal core) is uniformly heated from the interior. The pairs of parameters used fulfill the relation $\mathrm{Pr/E} = O(10)$ that, according to Refs. [17] and [18], ensures having periodic torsional solutions at the onset of convection with stress-free boundary conditions. The latter authors also proved that, for this ratio, the torsional modes are never preferred with nonslip boundary conditions. Since they appear at a Hopf bifurcation, which does not break the rotational invariance of the conductive state, the resulting flows are no longer rotating waves. Therefore to study the periodic solutions it is necessary to use time evolution codes to simulate their behavior or continuation methods for periodic orbits like those described in Refs. [22–24]. We adopt this latter approach, which, in addition to providing a complete description of the dependence of the properties of the solutions on the parameters, also allows us to obtain unstable states, which could be relevant in complex dynamics involving, for instance, mixed solutions or heteroclinic chains visiting several unstable invariant objects. The quasiperiodic and more complex solutions are computed by means of direct numerical simulations and analyzed using techniques of dynamical systems.

The remainder of the paper is organized as follows. In Sec. II the equations and the numerical method employed are briefly introduced. In addition, some tests on the performance of the codes are also shown. The Rayleigh number dependence of several dynamical and thermal properties of the torsional periodic orbits such as its kinetic energy, considering its toroidal and poloidal, or equatorially symmetric and antisymmetric parts, the helicity, the heat transport, etc., is studied in Sec. III. This part is an extension that complements the study presented in Ref. [18]. Section IV describes and analyzes the complex time dependence of the flows and their physical traits for higher values of Ra. Finally, remarks on the main results are included in Sec. V.

II. FORMULATION AND NUMERICAL METHODS

Thermal convection in an internally heated fluid sphere, subject to radial gravity $\mathbf{g} = -\gamma \boldsymbol{r}$, with $\gamma > 0$, and constant temperature T_o at the surface is considered. The Boussinesq approximation of the mass, momentum, and energy equations is written in the rotating frame of reference of the sphere. The centrifugal force is neglected since $\Omega^2/\gamma \ll 1$ such as happens, for instance, in the major planets and stars, and we take constant density in the Coriolis term. In addition, we consider the following scales: the radius, r_o, of the sphere for the distance, a viscous time r_o^2/ν, and $\nu^2/\gamma\alpha r_o^4$ for the temperature. The physical constants are the kinematic viscosity, ν, and the thermal expansion coefficient, α.

A general formulation with the velocity field written in terms of toroidal and poloidal velocity potentials, i.e., $\boldsymbol{v} = \boldsymbol{\nabla} \times (\Psi \boldsymbol{r}) + \boldsymbol{\nabla} \times \boldsymbol{\nabla} \times (\Phi \boldsymbol{r})$, is adopted in order to prepare the study of the 3D instabilities of the periodic torsional flows for a future work. The equations are linearized around the conduction state $\boldsymbol{v} = \mathbf{0}$ and $T_c(r)$, with $T_c(r) = T_o + \mathcal{S}(r_o^2 - r^2)/6\kappa$. The constant $\mathcal{S}$ is q/c_p, q being the rate of internal heat generation per unit mass, c_p the specific heat at constant pressure, and κ the thermal diffusivity. The equations are

$$(\partial_t - \Delta)\mathcal{L}_2\Psi = 2\mathrm{E}^{-1}\,(\partial_\varphi \Psi - \mathcal{Q}\Phi) - \boldsymbol{r} \cdot \boldsymbol{\nabla} \times (\boldsymbol{\omega} \times \boldsymbol{v}), \tag{1}$$

$$(\partial_t - \Delta)\mathcal{L}_2\Delta\Phi = 2\mathrm{E}^{-1}\,(\partial_\varphi \Delta\Phi + \mathcal{Q}\Psi) - \mathcal{L}_2\Theta + \boldsymbol{r} \cdot \boldsymbol{\nabla} \times \boldsymbol{\nabla} \times (\boldsymbol{\omega} \times \boldsymbol{v}), \tag{2}$$

$$(\mathrm{Pr}\partial_t - \Delta)\Theta = \mathrm{Ra}\mathcal{L}_2\Phi - \mathrm{Pr}(\boldsymbol{v} \cdot \boldsymbol{\nabla}\Theta), \tag{3}$$

where $\boldsymbol{r}$ is the position vector, $\boldsymbol{\omega} = \boldsymbol{\nabla} \times \boldsymbol{v}$ is the vorticity, $\Theta(r, \theta, \varphi) = T(r, \theta, \varphi) - T_c(r)$ is the temperature perturbation, and (r, θ, φ) are the spherical coordinates, θ measuring the colatitude.

The operators $\mathcal{L}_2$ and $\mathcal{Q}$ are defined as $\mathcal{L}_2 = -r^2\Delta + \partial_r(r^2\partial_r)$ and $\mathcal{Q} = r\cos\theta\Delta - (\mathcal{L}_2 + r\partial_r)(\cos\theta\partial_r - r^{-1}\sin\theta\partial_\theta)$. Since we look for axisymmetric solutions, all the derivatives ∂_φ are taken as zero in all the equations.

The nondimensional parameters are the Rayleigh, Prandtl, and Ekman numbers, defined as

$$\mathrm{Ra} = \frac{S\gamma\alpha r_o^6}{3\kappa^2\nu}, \quad \mathrm{Pr} = \frac{\nu}{\kappa}, \quad \text{and} \quad \mathrm{E} = \frac{\nu}{\Omega r_o^2}, \tag{4}$$

respectively. The Taylor number was used in Ref. [25], which is related to the Ekman number by $\mathrm{Ta} = \mathrm{E}^{-2}$.

Stress-free boundary conditions $\Phi = \partial_{rr}^2\Phi = \partial_r(\Psi/r) = 0$, and a perfectly conducting boundary, which means $\Theta = 0$ at $r = r_o$, are taken. At $r = 0$ only regularity conditions are required. The functions Φ, Ψ, and Θ are expanded in spherical harmonic series up to degree L as

$$X(r,\theta,t) = \sum_{l=0}^{L} X_l^0(r,t)P_l^0(\cos\theta),$$

where X represents any of them, P_l^0 being the normalized associated Legendre functions of degree l and order 0, which coincide with the spherical harmonics $Y_l^0(\theta,\varphi)$ and are independent of φ. Due to the indeterminacy of Φ and Ψ we take $\Phi_0^0 = \Psi_0^0 = 0$.

A collocation method on a Gauss-Lobatto mesh of $N+1$ points is used to discretize the equations radially. The regularity conditions imply (see, for instance, Ref. [26]) that $X_l^0(r,t) = r^l Z_l^0(r,t)$, with $Z_l^0(r,t)$ even and smooth. Therefore, if $l > 0$, X_l^0 and its radial derivatives up to order $l-1$ must vanish at $r = 0$, but we only enforce $X_l^0(r=0) = 0$ in the discretized radial differential operators, which include the boundary conditions. If $l = 0$ the only additional condition is $\partial_r X_0^0(r=0) = 0$. This is needed only for the temperature since $\Phi_l^0 = \Psi_l^0 = 0$. It was shown in Ref. [25] that imposing only these conditions is enough to obtain consistent results for the linear stability analysis of the conduction state, avoiding several types of spurious modes. In this way the set of equations (1)–(3) becomes a system,

$$\dot{\boldsymbol{u}} = \mathcal{L}\boldsymbol{u} + \mathcal{N}(\boldsymbol{u},\boldsymbol{u}), \tag{5}$$

of $(3L+1)(N-1)$ real ordinary differential equations (ODEs). The vector $\boldsymbol{u}$ contains the value of the amplitudes of the spherical harmonic expansions at the internal collocation nodes. The linear part $\mathcal{L}$ depends on the three nondimensional parameters (4). It has a diagonal block of dimension $N-1$ for Θ_0^0, followed by a block-tridiagonal part of L rows of blocks of dimension $3(N-1)$ for the rest of amplitudes, due to the structure of the operator $\mathcal{Q}$. The quadratic terms in $\mathcal{N}(\boldsymbol{u},\boldsymbol{u})$ come from the advection operators of the original equations. The stiff system of ODEs (5) was integrated by means of the fully implicit LSODPK solver of the ODEPACK package [27] or by a fifth-order semi-implicit method (IMEX) based on backward-differentiation-extrapolation formulas described, for instance, in Ref. [28]. Since stress-free boundary conditions are applied, conservation of the z component of the angular momentum

$$L_z(t) = \int_V r v_\varphi(t,r)\sin\theta\, dV \tag{6}$$

by the numerical code must be guaranteed. By substituting $v_\varphi = -\partial_\theta\Psi$, and after the spectral discretization, it turns out that

$$L_z(t) = 2\sqrt{6}\pi \int_0^{r_o} r^3\Psi_1^0(t,r)\, dr, \tag{7}$$

i.e., written in spherical harmonics the condition affects the coefficient of the normalized associate Legendre polynomial of first degree. Then the conservation of the angular momentum has been implemented by modifying the part of the vector field in Eq. (5) corresponding to this variable. Details on how it has been implemented can be found in the Appendix. The underlying idea is to add a small body force that compensates the drift of the angular momentum, instead of the frequently

used strategy of introducing shear forces by modifying the boundary conditions corresponding to Ψ. In this way by selecting $L_z(0) = 0$, and after time integrations of 300 viscous units or longer $L_z(t)$ belongs below 10^{-9}.

Several tests were made and the conclusion was that when E and Pr are not very small the IMEX method can be more efficient than the fully implicit LSODPK. However, in the cases shown in this article the latter proved to be less expensive from a computational point of view.

The periodic orbits of the system (5) are computed by solving the system of equations

$$\boldsymbol{u} - \boldsymbol{\phi}(T, \boldsymbol{u}, p) = 0, \tag{8}$$

$$g(\boldsymbol{u}, p) = 0 \tag{9}$$

for $(T, \boldsymbol{u}, p)$, where T is the period, p is a parameter of the problem that for the present calculations will be $p = \mathrm{Ra}$, $\boldsymbol{\phi}(t, \boldsymbol{u}, p)$ is the solution of (5) with $\boldsymbol{\phi}(0, \boldsymbol{u}, p) = \boldsymbol{u}$, and $g(\boldsymbol{u}, p) = 0$ is a phase condition to select just one point on each periodic orbit. It can be, for instance, the Poincaré condition $g(\boldsymbol{u}, p) = \dot{\boldsymbol{u}}(\boldsymbol{u}_0) \cdot (\boldsymbol{u} - \boldsymbol{u}_0) = 0$, where $\dot{\boldsymbol{u}}(\boldsymbol{u}_0)$ is the tangent to the last computed periodic orbit at the point obtained on it, $\boldsymbol{u}_0$. The details on how to compute the cycles and to obtain their stability (Floquet multipliers) can be found in Ref. [22] or in the more recent and detailed review on continuation methods for partial differential equations [24]. Here the spatiotemporal symmetries of the torsional periodic orbits were used to halve the integration time.

The curves of torsional solutions were traced as a function of Ra for $(\mathrm{E}, \mathrm{Pr}) = (10^{-3}, 10^{-2})$ and $(\mathrm{E}, \mathrm{Pr}) = (10^{-4}, 10^{-3})$. The global data represented in the corresponding plots correspond to physical properties averaged over the whole volume of the sphere, V, or boundary, S, and their time averages. The volume averages can be computed for a generic scalar function $f(t, r, \theta, \varphi)$ as

$$F(t) = \frac{1}{V}\int_V f(t, r, \theta, \varphi)\, dV = \frac{3\sqrt{2}}{2r_o}\int_0^{r_o} r^2 f_0^0(r, t)\, dr, \tag{10}$$

where f_l^m is the coefficient of order m and degree l of the expansion of the function f in spherical harmonics. Its time average and maximum are

$$\overline{F} = \frac{1}{T}\int_0^T F(t)\, dt, \quad \text{and} \quad F^{\max} = \max_{t\in[0,T]} F(t), \tag{11}$$

T being either the period of the torsional solution or the total integrated time when the solutions are not periodic. The time integral is approximated by the trapezoidal rule during the time integration.

The volume-averaged kinetic energy per unit mass, called from now on for simplicity kinetic energy, and the volume-averaged helicity (helicity for short) are

$$K(t) = \frac{1}{V}\int_V \frac{1}{2}\boldsymbol{v}\cdot\boldsymbol{v}\, dV \quad \text{and} \quad H(t) = \frac{1}{V}\int_V \boldsymbol{v}\cdot\boldsymbol{\omega}\, dV. \tag{12}$$

In the axisymmetric case ($\partial_\varphi = 0$) the toroidal-poloidal decomposition

$$\boldsymbol{v} = \boldsymbol{v}_T + \boldsymbol{v}_P = \boldsymbol{\nabla}\times(\Psi\mathbf{r}) + \boldsymbol{\nabla}\times\boldsymbol{\nabla}\times(\Phi\mathbf{r})$$

becomes

$$\boldsymbol{v}_T = -\partial_\theta\Psi\hat{e}_\varphi, \quad \boldsymbol{v}_P = \frac{1}{r}L_2\Phi\hat{e}_r + \frac{1}{r}\partial^2_{r\theta}(r\Phi)\hat{e}_\theta.$$

Then $\boldsymbol{v}_T$ contains the full azimuthal velocity, and $\boldsymbol{v}_P$ the full meridional part. Since they are orthogonal the kinetic energy and its time average can also be decomposed as $K = K_T + K_P$.

A second splitting $\boldsymbol{v} = \boldsymbol{v}_s + \boldsymbol{v}_a$, where $\boldsymbol{v}_s$ is the symmetric part of $\boldsymbol{v}$ with respect to the equator and $\boldsymbol{v}_a$ the antisymmetric part, is also possible. It can be seen that although $\boldsymbol{v}_s$ and $\boldsymbol{v}_a$ are not orthogonal the integral of $\boldsymbol{v}_s\cdot\boldsymbol{v}_a$ over V vanishes, and then $K = K_s + K_a$. Since the eigenfunction at the onset of convection is antisymmetric with respect to the equator, this decomposition will reflect very well the influence of the nonlinearity on the flow and the relative importance of the symmetry breaking.

TABLE I. First 16 Floquet multipliers of the torsional periodic solution for $\mathrm{Pr} = 10^{-2}$, $\mathrm{E} = 10^{-3}$, and $\mathrm{Ra} = 16\,010$.

Real part	Imaginary part	Modulus
−1.3393	±2.9555	3.2448
−1.4210	±0.7942	1.6279
0.0527	±1.3373	1.3383
0.7054	±0.7368	1.0200
−0.8653	±0.1061	0.8718
0.6359	0.0000	0.6359
0.2257	±0.5798	0.6222
0.5759	0.0000	0.5759
−0.3982	±0.2563	0.4736

The heat transport will be quantified with the Nusselt number, defined as the ratio of the total radial heat flux to the conductive heat flux, both averaged through the boundary of the sphere:

$$\mathrm{Nu}(t) = \frac{\langle J_T(t, r_o, \theta)\rangle_S}{\langle J_c(r_o)\rangle_S} = -\frac{\sqrt{2}\mathrm{Pr}}{2\mathrm{Ra}}\partial_r \Theta_0^0(t, r_o) + 1. \tag{13}$$

The brackets $\langle\ \rangle_S$ mean the surface integral evaluated at $r = r_o$. For the torsional time periodic solutions $\overline{H}$ is zero due to their spatiotemporal symmetries (see below), and $\overline{\mathrm{Nu}}$ is also zero due to the internal heating considered, consequently their maxima over a period, $\mathrm{Nu}^{\max} - 1$ and $H^{\max}$, will be taken as measure of heat transport. For nonperiodic flows the maxima is taken either for a time $T = 1/f$, f being the smallest frequency of the solution, or during a sufficiently long time, for which the averages defined above do not change. Notice that $\overline{\mathrm{Nu}} \approx 1$ also for quasiperiodic solutions since the trajectories of the orbits will pass as close as required to the initial condition after a sufficiently long time T'. As in the periodic case all the heat generated during this time must have been released to the exterior because the final state is now almost the same than the initial. The same holds for the conduction state, and then $\langle J_T(T', r_o, \theta)\rangle_S = \langle J_c(r_o)\rangle_S$. To overcome the problem of having $\overline{\mathrm{Nu}} \approx 1$ for any flow, other authors, for instance in Ref. [29], measure the efficiency of the heat transport as the ratio between the total heat flux and the heat flux that would correspond to a modified conductive state with the temperature at the center $T_c(r = 0) + \Theta(r = 0)$.

To check the reliability of the results the quantities previously defined were computed for the periodic solution of parameters $\mathrm{Pr} = 10^{-2}$, $\mathrm{E} = 10^{-3}$, and $\mathrm{Ra} = 16\,010$, by changing the number of radial collocation points, N, and the maximum degree of the spherical harmonics, L. It was selected far from the critical point $\mathrm{Ra_c} = 7366$ of the beginning of the periodic regime, and after four bifurcations on the branch of periodic solutions. Table I shows the sixteen leading Floquet multipliers of the solution with four complex-conjugate pairs outside the unit circle, for $N = 30$ and $L = 50$. Table II shows the comparison of the period of the orbit, its time-averaged symmetric and antisymmetric kinetic energies, its time-averaged poloidal and toroidal kinetic energies, and the maximum Nusselt number and helicity over a period. The relative difference between the maximum and minimum values of each column of the table ($\mathrm{Nu}^{\max} - 1$ for the Nusselt number) is below 0.2%. That of resolution $N = 30$ and $L = 50$ is even below, so these intermediate truncation parameters were used for the rest of the calculations.

III. RESULTS: PERIODIC SOLUTIONS

The variation of the physical properties included in Table II with Ra is described below. Figure 1 shows the variation of the period with Ra for the two pairs of parameters studied. In this paper solid lines mean stable solutions and dashed lines unstable. As said before, the oscillations begin

TABLE II. Comparison of the period, the time-averaged symmetric and antisymmetric kinetic energies, the time-averaged poloidal and toroidal energies, and the maximum Nusselt number and helicity over a period, for several resolutions. The parameters of the periodic solution are $\mathrm{Pr} = 10^{-2}$, $\mathrm{E} = 10^{-3}$ and $\mathrm{Ra} = 16\,010$.

N	L	$10^3 T$	$10^{-4}\overline{K}_s$	$10^{-4}\overline{K}_a$	$10^{-4}\overline{K}_T$	$10^{-4}\overline{K}_P$	$\mathrm{Nu}^{\max}$	$10^{-5}H^{\max}$
20	40	7.6897	2.5273	6.8042	4.9517	4.3798	1.020800	5.7996
20	50	7.6901	2.5289	6.8059	4.9536	4.3812	1.020805	5.8019
30	40	7.6916	2.5291	6.7942	4.9487	4.3747	1.020793	5.7994
30	50	7.6921	2.5306	6.7955	4.9503	4.3758	1.020797	5.8015
30	60	7.6923	2.5310	6.7960	4.9508	4.3762	1.020799	5.8018
40	50	7.6922	2.5306	6.7950	4.9501	4.3755	1.020797	5.8014
40	60	7.6923	2.5309	6.7955	4.9505	4.3759	1.020798	5.8017

at $\mathrm{Ra_c} = 7366$ for $\mathrm{E} = 10^{-3}$ and $\mathrm{Pr} = 10^{-2}$. The branch of periodic solutions loses stability at a Neimark-Sacker bifurcation (Hopf bifurcation of periodic orbits) at $\mathrm{Ra} = 12\,209$, and it never regains it. The curve has two folds at $\mathrm{Ra} = 12\,217$ and $\mathrm{Ra} = 11\,840$ in its unstable part. The period has a small decrease up to the first fold and then it grows quickly around a 11%. For $\mathrm{E} = 10^{-4}$ and $\mathrm{Pr} = 10^{-3}$ the onset of convection takes place at $\mathrm{Ra_c} = 7640$. The periodic regime becomes unstable sooner, at $\mathrm{Ra} = 7921$, also through a Neimark-Sacker bifurcation, so the range of Ra computed is shorter than before. In the interval considered the period decreases monotononically from $T = 7.0296 \times 10^{-4}$ even in the unstable part of the curve. The period of the orbits is order E, namely, the oscillations are faster when E decreases.

Figures 2 and 3 show the variation of the time average of the toroidal and poloidal components of the kinetic energy, and that of its equatorial symmetric and antisymmetric parts, with Ra. For $\mathrm{E} = 10^{-3}$ and $\mathrm{Pr} = 10^{-2}$ the toroidal and poloidal curves of the kinetic energies almost overlap up to the second fold. After this point, the toroidal overcomes the poloidal part of $\overline{K}$, and both reach a maximum and slowly decrease. For the lower parameters $\mathrm{E} = 10^{-4}$ and $\mathrm{Pr} = 10^{-3}$ both curves are very close in the interval of Ra considered. The behavior of the branches of symmetric and antisymmetric $\overline{K}$ is completely different from the onset (see Fig. 3). At the Hopf bifurcation the eigenfunction is fully antisymmetric, and the symmetric part grows due to the quadratic terms of the equations. For $\mathrm{E} = 10^{-3}$ and $\mathrm{Pr} = 10^{-2}$, it continues increasing very slowly in the stable part of the branch up to the first fold, then the ratio $\overline{K}_s/\overline{K}_a$ increases from 0.1 to 0.2 between the two folds and grows slowly up to 0.4 at $\mathrm{Ra} = 18\,000$. For the lower set of parameters, $\mathrm{E} = 10^{-4}$ and $\mathrm{Pr} = 10^{-3}$, the ratio $\overline{K}_s/\overline{K}_a$ increases monotonically from 0 to close to 0.05 at $\mathrm{Ra} = 11\,000$.

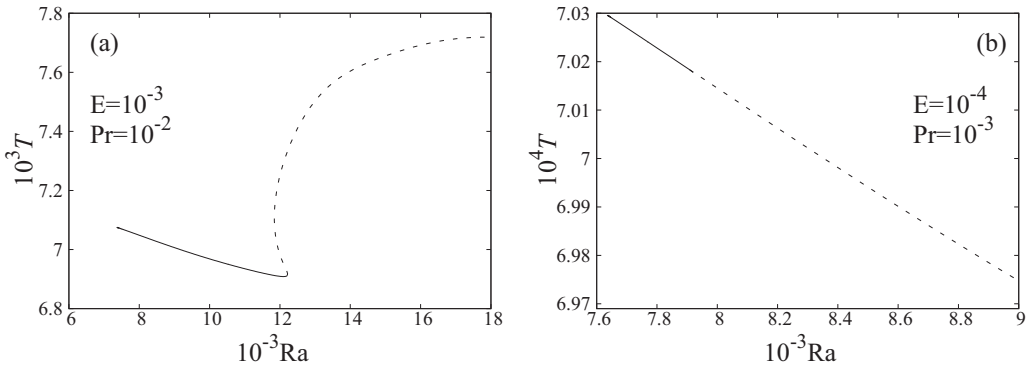

FIG. 1. Period along the branches of periodic orbits versus the Rayleigh number. Solid lines mean stable solutions and dashed lines unstable.

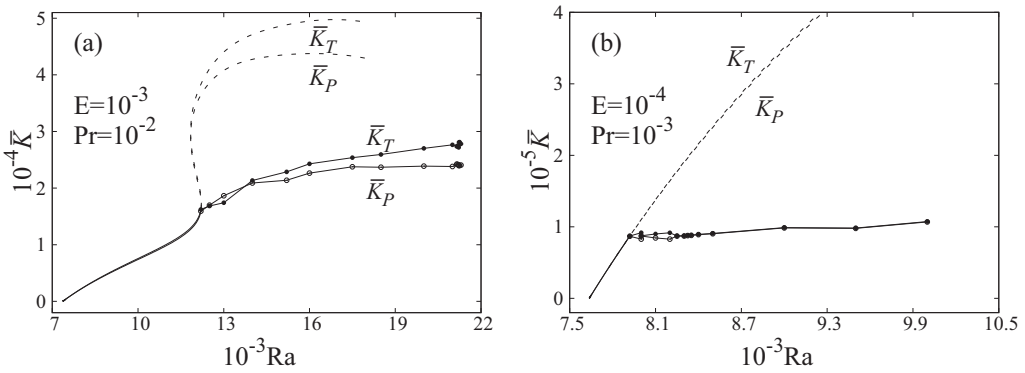

FIG. 2. (a, b) Decomposition of the kinetic energy into its toroidal and poloidal components versus the Rayleigh number. Solid lines mean stable solutions and dashed lines unstable. The lines following the circles correspond to stable nonperiodic solutions. Full circles indicate $\overline{K}_T$, and empty $\overline{K}_P$.

Summarizing, it is found that, in any case, the time- and volume-averaged kinetic energy of the stable periodic torsional solutions is mainly antisymmetric, and it splits equally in the poloidal and the toroidal components. This does not mean that the latter relation be fulfilled at any time instant, as will be seen later.

Figure 4 shows the variation of the Nusselt number and the helicity with Ra, respectively. As said before their maxima over the period are plotted. As can be seen in the figure $\mathrm{Nu}^{\max} - 1$ is very small, indicating that the torsional flows are not more efficient for heat transport than the conduction state, not only time averaged, but also pointwise. In addition, the instantaneous heat flux across the outer sphere decreases with E. On the other hand, the helicity is large, but since the solutions are symmetric cycles (S cycles), i.e.,

$$v_r(t, r, \theta, \varphi) = v_r(t + T/2, r, \pi - \theta, \varphi), \tag{14}$$

$$v_\theta(t, r, \theta, \varphi) = -v_\theta(t + T/2, r, \pi - \theta, \varphi), \tag{15}$$

$$v_\varphi(t, r, \theta, \varphi) = v_\varphi(t + T/2, r, \pi - \theta, \varphi), \tag{16}$$

$$\Theta(t, r, \theta, \varphi) = \Theta(t + T/2, r, \pi - \theta, \varphi), \tag{17}$$

they have zero time-averaged helicity.

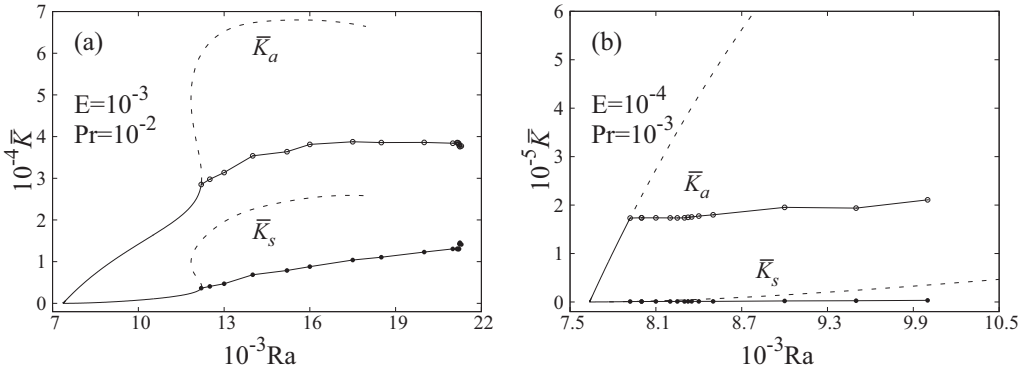

FIG. 3. (a, b) Decomposition of the kinetic energy into its symmetric and antisymmetric parts versus the Rayleigh number. The symbols and type of lines are the same as in Fig. 2.

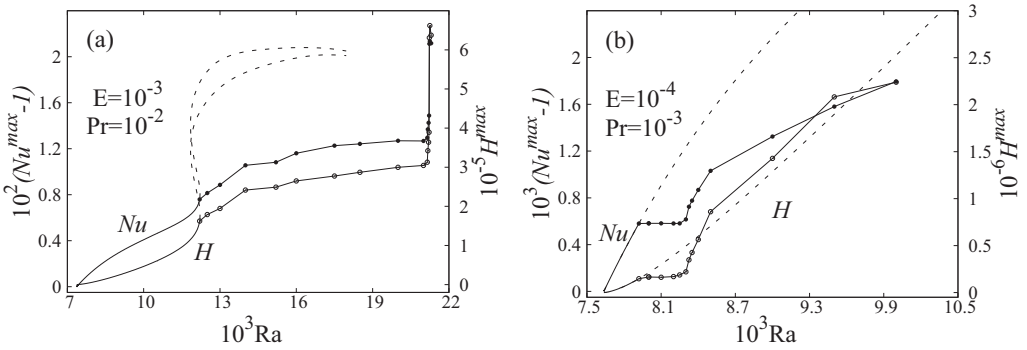

FIG. 4. (a, b) Maximum Nusselt (left vertical axis) and helicity (right vertical axis) numbers along the branches of solutions versus the Rayleigh number. The symbols and type of lines are the same as in Fig. 2.

Time evolutions over a period, T, (not shown here) of several macroscopic magnitudes for the torsional solutions at the bifurcation points where the branches of periodic orbits lose stability were analyzed. For $E = 10^{-4}$, $\mathrm{Pr} = 10^{-3}$, and $\mathrm{Ra} = 7921$ the distance to the initial Hopf bifurcation ($\mathrm{Ra} = 7640$) is small. Then the behavior is very close to that of the eigenfunction at the onset of convection (see Ref. [17]), with an almost complete exchange of kinetic energy between the toroidal and poloidal components because they are a quarter period out of phase, their mean value and amplitude are the same, and the minimum is almost zero. This is why the two curves represented in each plot of Fig. 2 overlap, except for $\mathrm{E} = 10^{-3}$ after the second fold. Moreover, $125 < K_a/K_s < 300$ in a period. On the other hand, the time evolution for $E = 10^{-3}$, $\mathrm{Pr} = 10^{-2}$, $\mathrm{Ra} = 12\,209$ shows that the interchange between K_T and K_P is not total, K_T never reaching zero. Moreover, $6 < K_a/K_s < 10$. The ratio is lower because the solution is further from the onset at $\mathrm{Ra} = 7366$. In any case, the time average of Nu and H are zero, while the instantaneous heat transport is higher for $E = 10^{-3}$ due to the higher distance to $\mathrm{Ra_c}$.

The behavior of the torsional periodic orbits far from the onset is illustrated in Fig. 5 with the projection of Θ and the velocity field on spherical, equatorial, and meridional surfaces for a period, respectively. The sections where the projections are taken are indicated on the surfaces. The evolution of Θ, the full temperature and the kinetic energy can also be seen in animations 1, 2, and 3 of the Supplemental Material [30], respectively. In any case, the color intensity of the snapshots and the length of the arrows of the velocity field are selected relative to the global maximum of the full period. They are ordered so that those in the same row differ by $T/2$. In this way it is easy to check that the orbit is symmetric, i.e., it fulfills relations (14)–(16) and (17) and that the nonlinear torsional solutions break the antisymmetry of the eigenfunctions. However, to see well the details of the changes of the velocity field and of the temperature perturbation it is better to look at the additional material. The interchange of sign of the fields at each semiperiod always takes place when Θ reach a minimum in both hemispheres. When the amplitude of Θ increases the hot (cold) fluid grows and expands in the opposite hemisphere, from the pole to the equator. The arrows of the velocity field always point to the hottest fluid (red online), and they become tangent to the parallels occupied by the hot fluid when the intensity goes to the minimum. The interchange occurs quickly, between $t = 3T/8$ and $T/2$, and $t = 7T/8$ and $t = T$ in Fig. 5. The temperature perturbation gives rise to a vertical oscillation of the total temperature in the hottest interior of the self-gravitating sphere (see animation 2 [30], mainly the meridional section). It increases to the north (south) pole when the velocity field points upwards (downwards). The maximum of the kinetic energy peaks, at any time, in the surface of the sphere, oscillating between the high latitudes of both hemispheres, from $\theta \approx 40^o$ to 140^o. The maxima with respect to time are located at these extreme points (see animation 3 [30]). These animations show very well the latitudinal propagation of the energy and the axial displacement of the hot nucleus.

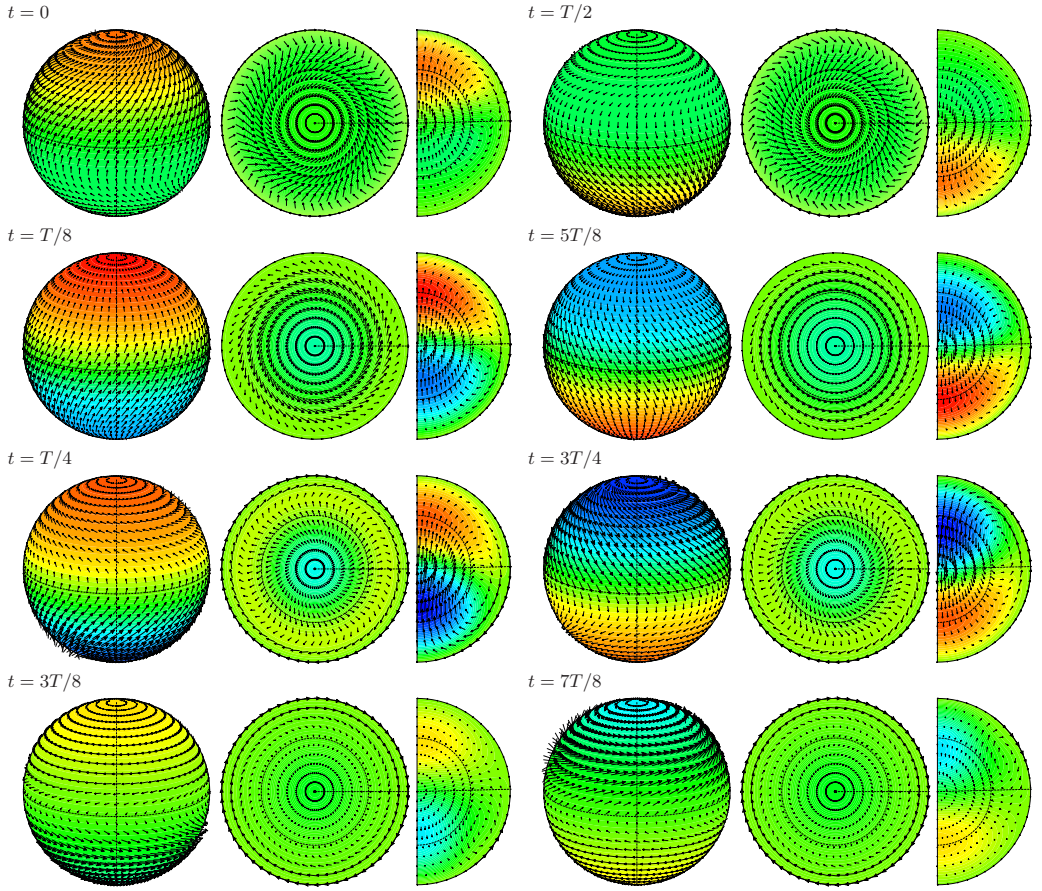

FIG. 5. Snapshots of the velocity field (arrows) superposed to the contour plots of the temperature for a period of oscillation of a stable solution of $E = 10^{-3}$, $Pr = 10^{-2}$, and $Ra = 12\,209$. At left from top to bottom $t = 0$, $T/8$, $T/4$, $3T/8$, and at right from top to bottom $t = T/2$, $5T/8$, $3T/4$, $7T/8$. The radial, equatorial, and meridional lines indicate the place where the sections are taken.

Concerning the robustness of the continuation and stability methods, Fig. 6 shows the leading Floquet multipliers at the first Neimark-Sacker bifurcation points and their trajectories for an interval of Ra containing them. The Floquet multipliers are the eigenvalues of the Jacobian of the Poincaré map. They give information on the stability of the periodic orbits and on the linearized dynamics around them. When all the multipliers are inside the unit circle the periodic orbit is asymptotically stable. A change of its stability takes place when a multiplier crosses out the circle. The corresponding eigenfunction gives information about the structure of the solutions on the emerging branch. The main difference between the two spectra of Fig. 6 is the clustering of the multipliers. For $E = 10^{-3}$ and $Ra = 12\,209$ only the modulus of the first 17 multipliers is higher than 0.35, while for $E = 10^{-4}$ and $Ra = 7921$, the modulus of the first 31 is larger than 0.82. For this reason the solutions for the lower E and Pr are much more difficult to compute. The Newton-Krylov method used to find them is very fast for very clustered spectra with multipliers not too close to $+1$. When they spread, the number of iterations required by the linear solver and, consequently, the required dimension of the Krylov subspace increase. In the second case several multipliers move along paths almost parallel to the unit circle, remaining very close to it when Ra is increased. Moreover, there are always several multipliers near $+1$, making the Jacobian of the system (8) close to singular, and thus the convergence of Newton's method also slows down. This

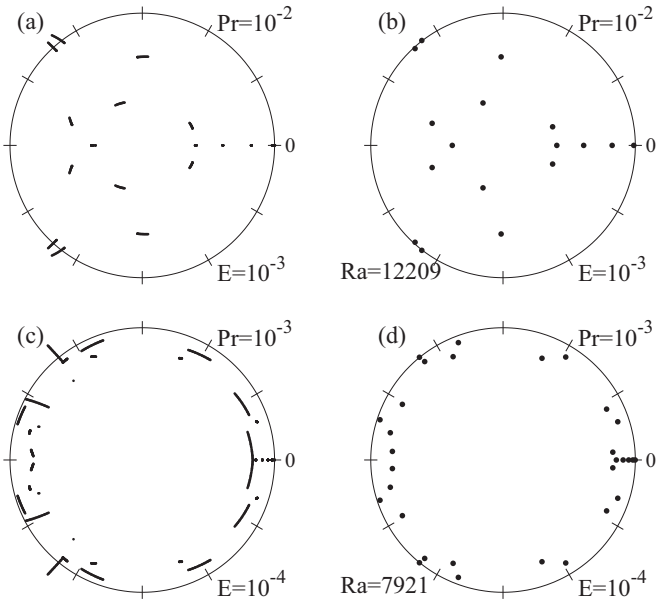

FIG. 6. (a, c) Trajectories of the Floquet multipliers spanning along Ra $\in$ [12 192, 12 243] for E $= 10^{-3}$ (17 multipliers), and Ra $\in$ [7806, 8330] for E $= 10^{-4}$ (31 multipliers). (b, d) Floquet multipliers at the bifurcation points. The phases on the unit circle are signaled every $\pi/6$, with the origin in the horizontal axis.

change in the spectrum foretell that computations at lower Pr and E would be extremely expensive. For instance, the computation of a periodic torsional solution, with a 10^{-6} relative error in Newton's method, using a serial continuation code executed on a Intel Xeon E5-2680 processor at 2.5 GHz has a average cost of 14 minutes at E $= 10^{-3}$ and 55 at E $= 10^{-4}$. Corcerning the stability of these solutions, the computation of 10 multipliers with a relative error of 10^{-6} takes 24 minutes in the first case and 55 in the second.

IV. DYNAMICS ABOVE THE NEIMARK-SACKER BIFURCATIONS

The dynamics above the critical Neimark-Sacker points where the periodic orbits lose stability is very different in the two cases studied in the preceding section.

A. Dynamics for E $= 10^{-3}$ and Pr $= 10^{-2}$

For E $= 10^{-3}$ and Pr $= 10^{-2}$ a second frequency, f_2, appears at the Neimark-Sacker bifurcation (Ra $=$ 12 209), giving rise to quasiperiodic orbits, stable to axisymmetric perturbations for a wide range of Ra. The new frequency of the solution at the transition point can be determined from the stability analysis of the periodic orbit at the critical point by calculating the rotation number $\rho = \beta/2\pi$, β being the phase of the Floquet multiplier. The second frequency is then $f_2 = \rho f_1$ with f_1 the frequency of the periodic orbit. This number is very useful to identify the second frequency of the new branch of solutions and clarify the time spectra of the quasiperiodic orbits. In one of these spectra f_2 and linear combinations of f_1 and f_2 usually appear. In the above case, $\rho = 0.3677$, $f_1 = 144.66$, and $f_2 = 53.19$. The bifurcated stable quasiperiodic trajectories fill densely two-dimensional (2D) surfaces (invariant tori). When $f1/f2$ becomes rational intervals of resonance appear, in which this ratio is locked, and the orbits on the tori are attracted to periodic regimes. In a generic Ruelle-Takens scenario these tori are broken when a third frequency appears

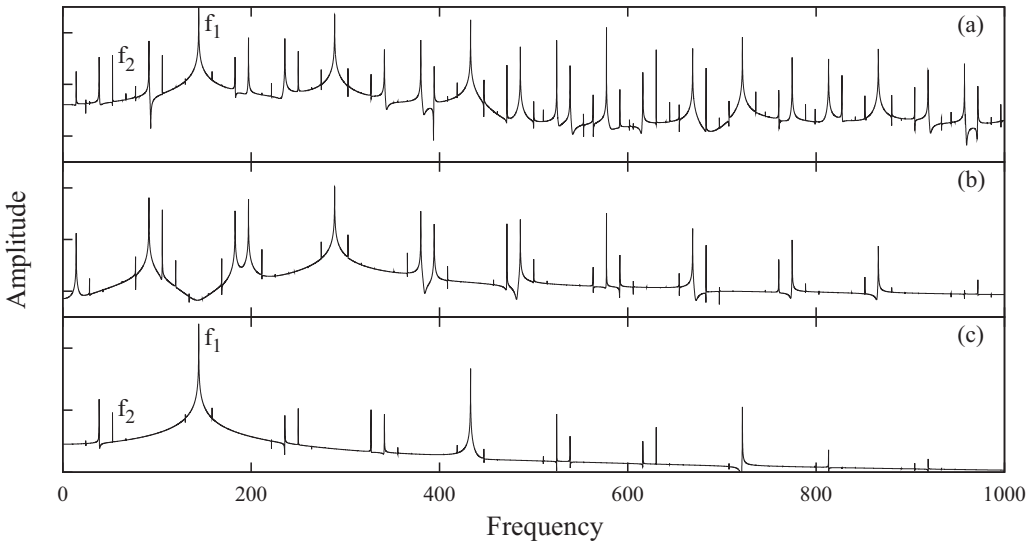

FIG. 7. Spectra of frequencies of the solution found at Ra = 12 500. (a) The colatitudinal component of the velocity field $v_\theta(r_o, \pi/6, \varphi)$, (b) $\Psi_1^0(r_m)$, with $r_m = r_o/2$, and (c) $\Phi_1^0(r_m)$.

and chaos develops. In the presence of spatiotemporal symmetries, as in the current problem, it is still possible to have, before chaos, quasiperiodic orbits on 3D tori.

The full spectrum of frequencies of one of this torus near the bifurcation point (Ra = 12 500) is illustrated in Fig. 7(a) by means of the colatitudinal component of the velocity field $v_\theta(r, \theta, \varphi) = v_\theta(r_o, \pi/6, \varphi)$. The spectra of the coefficients of the spherical harmonics show only part of that of the physical velocity, and sometimes some of the fundamental frequencies can only be derived from their combinations. For instance, in the spectrum of Fig. 7(b), corresponding to $\Psi_1^0(r_m)$, with $r_m = r_o/2$, the peaks of f_1 and f_2 are missing; however, they appear in Fig. 7(c), corresponding to $\Phi_1^0(r_m)$, and the curve is quite clean. It could appear that the optimal spectrum to follow the evolution of the tori should be that of the velocity field; however, when Ra is increased, it becomes too complicated to follow the new frequencies clearly. Consequently, the spectra of $\Phi_1^0(r_m)$ will be shown for $E = 10^{-3}$.

The change of the spectra and the development of the tori up to the loss of their stability are represented in Fig. 8 and in the Poincaré sections of Fig. 9. The latter show the intersections of an orbit of the discretized dynamical system with a certain hyperplane. These intersections can be shown in two or three dimensions and help to clarify the number of inconmensurable frequencies of the trajectories before turbulence. In Fig. 9 the section corresponds to the hyperplane $\Phi_1^0(r_m) = 0$. It is worth noting that this spherical harmonic coefficient accounts for most of the poloidal part of the velocity field, so the section selects a time at which it is almost toroidal. The spectrum of Fig. 8(a) and the dot of Fig. 9(a) correspond to a stable periodic solution very near to the bifurcation point (Ra = 12 200). Figures 8(b)–8(g) summarize the intricacy of the spectra when the tori increase their size. At Ra = 12 500, the frequencies are $f_1 = 144.34$ and $f_2 = 52.85$. Figure 8(c) corresponds to the spectrum of the seventh torus of Fig. 9(a), which is almost resonant, with frequencies $f_1 = 141.17$ and $f_2 = 49.84$. The new peaks grow around those of maximum amplitude, reminiscent of a comb shape. When Ra increases the second frequency decreases faster than the first, and, out of resonance, the secondary peaks get closer to the tallest, as happens in Figs. 8(d) and 8(e). By increasing Ra the two-tori increase their size [see Fig. 9(a)] and undulate, before the appearance of a small third frequency, f_3, between Ra = 21 000 and Ra = 21 150, giving rise to a three-torus, i.e., to an oscillatory solution with three independent frequencies [see the thin band in Fig. 9(a)].

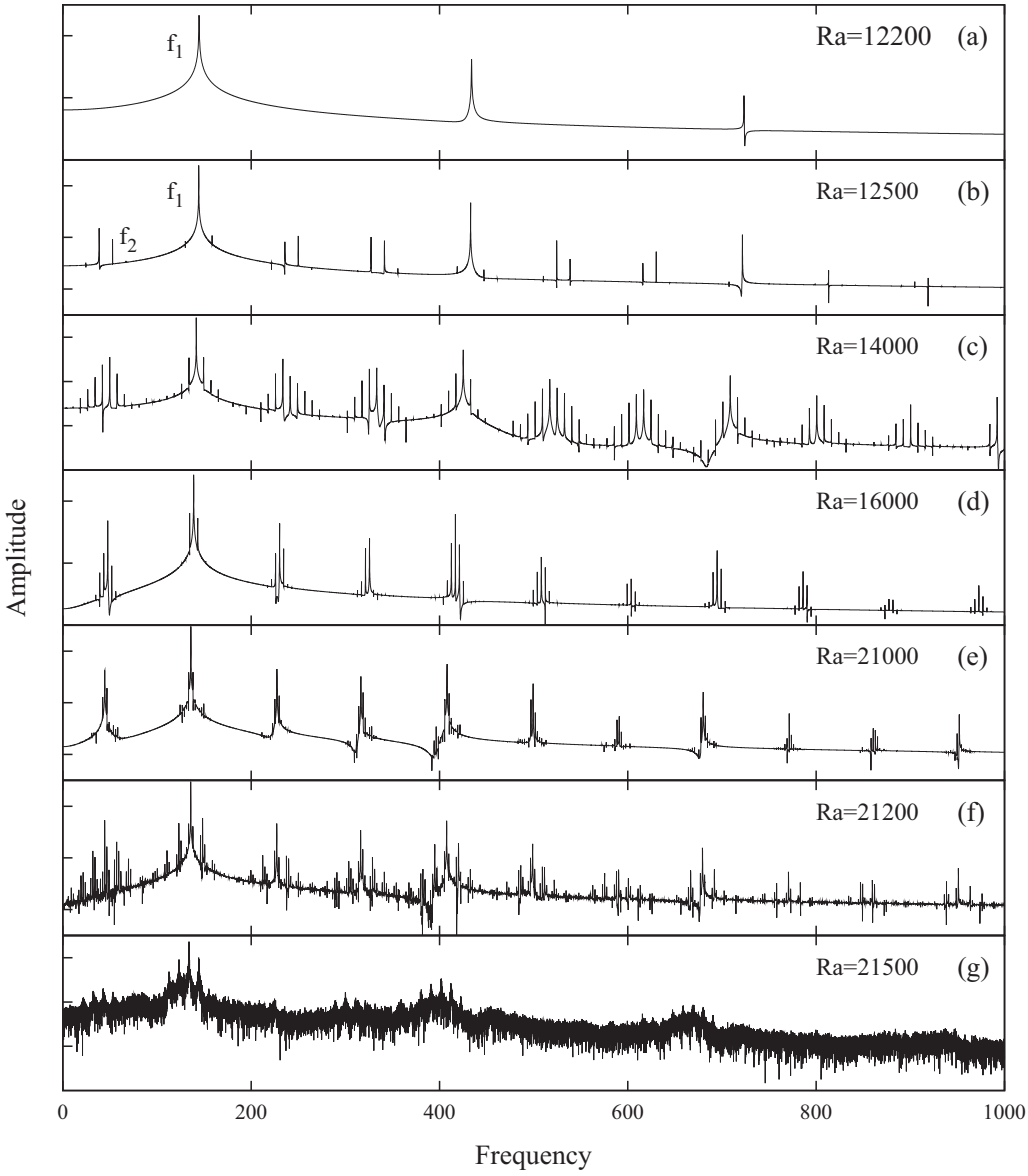

FIG. 8. Evolution of the spectrum of frequencies of $\Phi_1^0(r_m)$, with $r_m = r_o/2$, from a periodic orbit to temporal chaos.

In a 3D representation the Poincaré section of a three-torus fills a 3D surface. Three of the tori computed are shown in Fig. 9(b). The smallest, which corresponds to Ra = 21 150, has frequencies $f_1 = 135.94$, $f_2 = 44.51$, and $f_3 = 2.394$. A typical spectrum for these solutions is shown in Fig. 8(f). Although it seems quite noisy, each peak can be written as a combination of three independent frequencies with relative errors below 2×10^{-5}. From this points f_1 and f_2 remain almost constant, while f_3 decreases. Finally, the tori lose stabilility, near Ra = 21 220, giving rise temporal chaotic attractors, represented by the cloud of points of Fig. 9(b). The spectrum of the chaotic attractors is very noisy [Fig. 8(g)], but it retains a remnant of the two main peaks and their multiples.

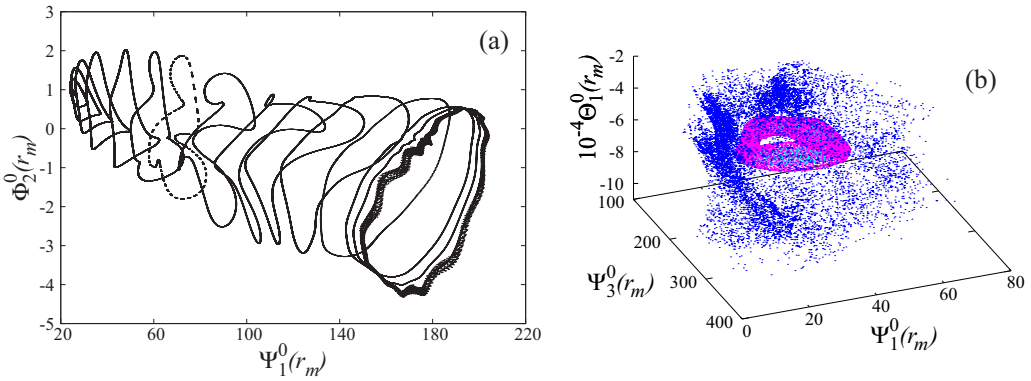

FIG. 9. (a) Poincaré sections taken at $\Phi_1^0(r_m) = 0$, for $E = 10^{-3}$, $Pr = 10^{-2}$, showing the evolution of the shape of the two-tori up to the appearance of the third frequency. The Rayleigh numbers are 12 200, 12 300, 12 500, 12 700, 13 000, 13 400, 13 700, 14 000, 14 400, 15 200, 16 000, 17 000, 18 500, 20 000, 20 500, 21 000, 21 150; (b) evolution of the three-tori up to the appearance of temporal chaotic solutions for Ra = 21 150, 21 170, 21 200, and 21 250.

Since the periodic torsional oscillations are S cycles the two-tori emerging when they lose stability are symmetric as sets [31]. So, when they in turn unstabilize, the third Hopf bifurcation gives rise to stable three-tori.

The above transitions modulate the amplitude of the periodic oscillations varying the mean and maximum values of K, H, and Nu. The mean values of some nonperiodic solutions versus Ra are represented in Figs. 2(a), 3(a), and 4(a) with circles connected with solid lines. For the quasiperiodic orbits, they have been computed by taking the average for a time $1/f_2$, for the solutions with three frequencies for a time $1/f_3$, and for the chaotic attractors for a time $t \gg 1/f_3$. In addition, the averaged quantities on some tori were recalculated by doubling the time of integration, and for the chaotic trajectories this time was increased according to the value of Ra until obtaining a near-constant value.

The averaged toroidal and poloidal components of the kinetic energy, $\overline{K}_T$ and $\overline{K}_P$ split at the Neimark-Sacker bifurcation like those of the periodic orbits after the second fold in the already unstable curve. At the beginning the poloidal component becomes larger than the toroidal [see Fig. 2(a)], but at the almost resonant orbit at Ra = 14 000 the curves cross, and from this point $\overline{K}_T$ is larger, as for the periodic orbits. While $\overline{K}_P$ is close to constant from Ra > 17 000, $\overline{K}_T$ increases slightly up to Ra > 21 000 when the three-tori and temporal chaotic solutions appear (cloud of points at the end of the branches).

The curves of the averaged symmetric part of the kinetic energy, $\overline{K}_s$, and the beginning of the antisymmetric part, $\overline{K}_a$, keep the slopes of the stable periodic solutions. Then the latter becomes almost horizontal [see Fig. 3(a)]. The chaotic solutions give rise to a moderate growth of $\overline{K}_s$ and fall of $\overline{K}_a$.

The maximum values of the Nusselt number, $\mathrm{Nu}^{\max}$, and those of the helicity, $H^{\max}$, of the quasiperiodic solutions follow the initial slope of the stable branches of periodic orbits. However, from Ra > 14 000 the slope decreases up to the starting of the complex dynamics. From Ra > 21 000, the solutions with three basic frequencies [first four points on the vertical line in Fig. 4(a)] and mainly the chaotic solutions (next three points on the same line) increase abruptly their maximum amplitude. However, the mean values of Nu and H are in any case very small.

B. Dynamics for $E = 10^{-4}$ and $Pr = 10^{-3}$

Because of the low value of the parameters with respect to the preceding case ($E = 10^{-4}$ and $Pr = 10^{-3}$), the periodic orbits lose stability in a Hopf bifurcation at 7921, giving rise to a stable

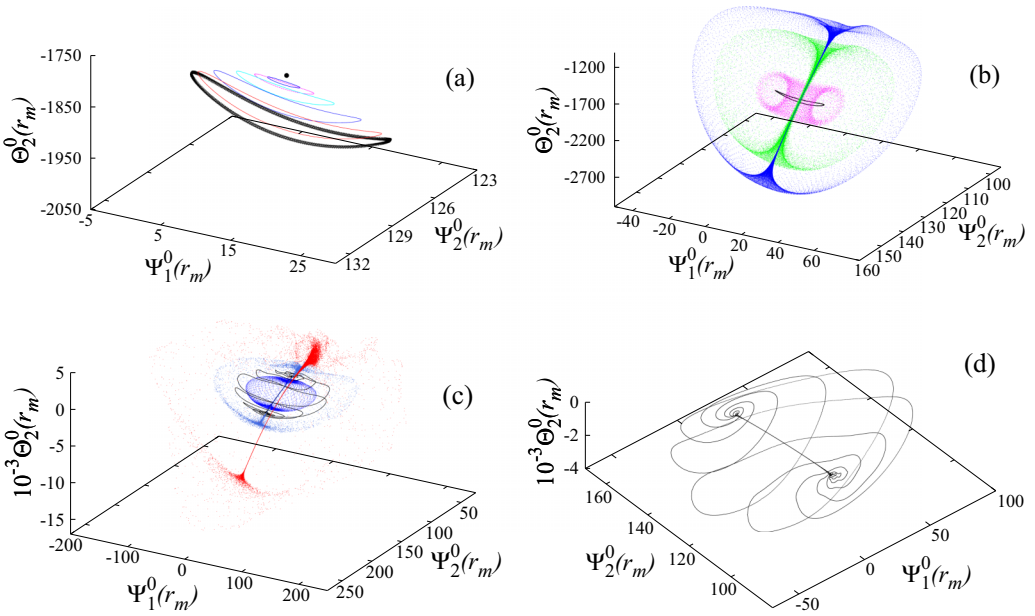

FIG. 10. (a) Poincaré sections taken at $\Phi_1^0(r_m) = 0$, for $E = 10^{-4}$, $Pr = 10^{-3}$, showing the evolution of the shape of the two-tori up to the appearance of the third frequency. The parameters are Ra = 7921, 7930, 7950, 8000, 8100, 8200, and 8250. (b) Enlargement of the three-tori. The parameters are Ra = 8250, 8300, 8325, and 8350. (c) Transition to temporal chaos showing the three-tori found at Ra = 8350 and at Ra = 8400, and the chaotic attractors at Ra = 8500 and Ra = 10 000. (d) Detail of the resonant torus at Ra = 8400.

(to axisymmetric perturbations) supercritical branch of two-tori of second frequency $f_2 = 511.27$, given by the rotation number $\rho = 0.3587$ and the frequency of the orbit at the bifurcation point $f_1 = 1424.95$. Their range of stability is very short since near Ra = 8200 the branch loses stability in a new Hopf bifurcation giving rise to supercritical three-tori. Figure 10(a) shows the growth of the two-torus. The main two frequencies remain almost constant until the appearance of temporal chaos. For instance, at Ra = 8100 they are $f_1 = 1424.88$, $f_2 = 511.11$, and at Ra = 8200, $f_1 = 1424.85$ and $f_2 = 511.10$, corresponding to the largest two-torus of Fig. 10(a) before the branch loses stability. However, as expected, some quasiresonant two-tori were found by increasing the parameter.

The frequencies of the three-torus at Ra = 8250 [wide band of Fig. 10(a)], near the third Hopf bifurcation, are $f_1 = 1424.83$, $f_2 = 511.09$, and $f_3 = 3.145$. Typical frequency spectra are shown in Figs. 11(a)–11(c). Each row shows a superposition of the spectrum of the coefficients $\Phi_1^0(r_m)$ (lower curve) and $\Psi_1^0(r_m)$, plotted to emphasize the peak f_3, which can be seen directly only in the latter. Since f_3 is very small in comparison with f_1 and f_2, the linear combinations of frequencies remain clustered around the initial peaks [see Figs. 11(d) and 11(e)]. As before, each of them was obtained as function of the basic three with little error. The third frequency oscillates in the interval $2 < f_3 < 4$, and, in addition, it halves after Ra = 8325. For instance, at Ra = 8350, $f_1 = 1424.83$, $f_2 = 511.10$, $f_3 = 3.831$, and $f_3/2 = 1.915$ is already visible in the spectrum. However, by increasing Ra the three-tori undergo a big enlargement and change of shape from Ra = 8300, illustrated in Fig. 10(b). The three-tori pass through resonant zones. For instance, the third torus of Fig. 10(c) (black online) is resonant, so its Poincaré section consists of closed curves on a 3D surface [see also Fig. 10(d)]. In this case the Poincaré section is a spiral of three arms. The range of stability of the three-tori is also very short, but when they lose stability a chaotic attractor appears, which maintains the structure of the three-tori, with its size still increasing with the parameter. See, for

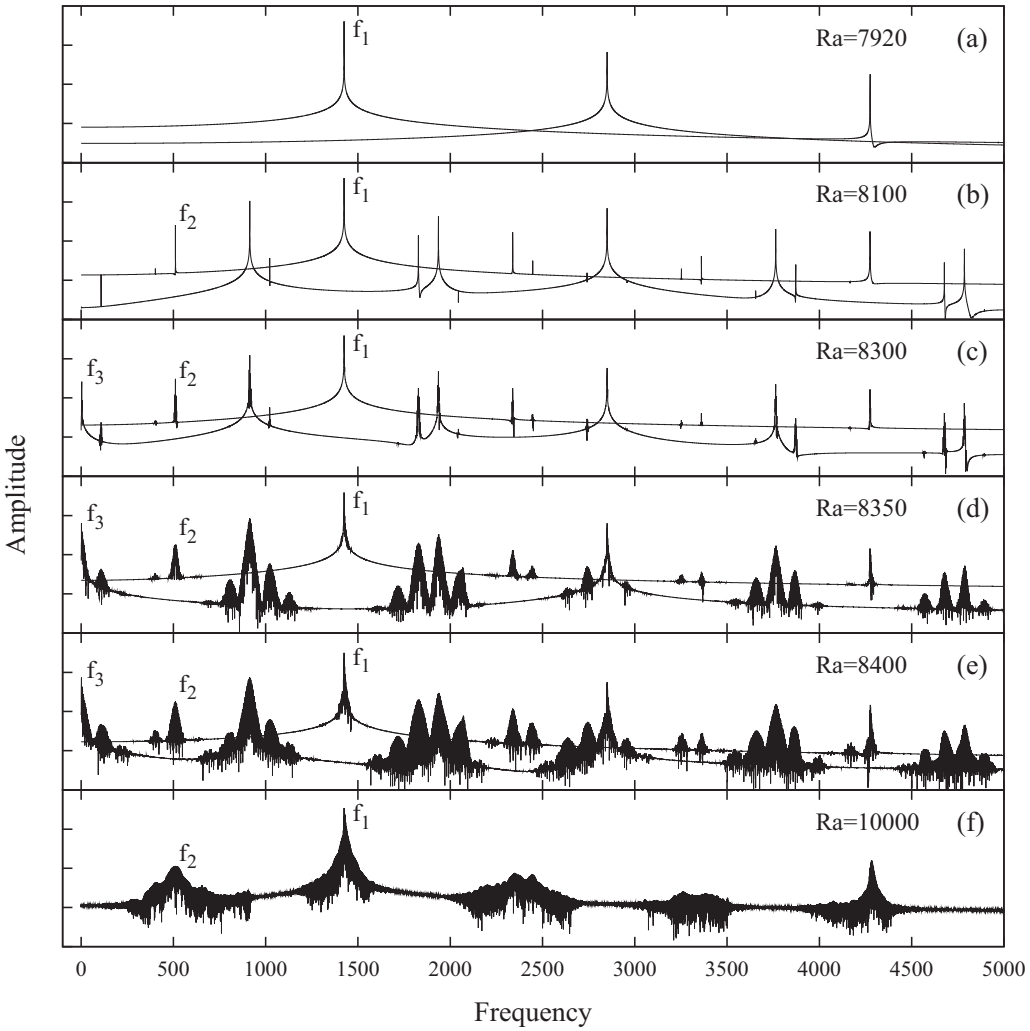

FIG. 11. (a–e) Evolution of the spectrum of frequencies of $\Psi_1^0(r_m)$ (upper spectra) and $\Phi_1^0(r_m)$ (lower spectra), with $r_m = r_o/2$, and (f) of $\Psi_1^0(r_m)$, from a periodic orbit to temporal chaos. The parameters are $E = 10^{-4}$, $Pr = 10^{-3}$.

instance, the two largest attractors shown in Fig. 10(c), for $Ra = 8500$ and $Ra = 10\,000$. Their distinctive characteristic is the complexity of the spectrum. It exhibits a continuum of frequencies [see Fig. 11(f)], which is not possible to describe in terms of only three fundamental frequencies.

As can be seen in Fig. 12, showing the temporal series of the velocity field and the perturbation of the temperature of these attractors, the two- and small three-tori are perturbations of the torsional periodic solutions, but after the change of shape, regular transients are found that slowly reach a high amplitude (compared to that of the periodic orbits) followed by a fast and drastic reduction. The origin of this dynamics can be visualized by plotting trajectories together with their preceding Poincaré sections, in 3D projections (see Fig. 13). When the attractors increase their size, they approach the unstable manifold of a periodic orbit. In Fig. 13(a) two portions of a trajectory (shown with dots for clarity) have been drawn only when it is close to one of the two unstable periodic orbits it approaches. They coincide with the accumulation of points of the Poincaré section (blue dots online). The full trajectory is displayed in Fig. 13(b), showing a 2D annular manifold limited

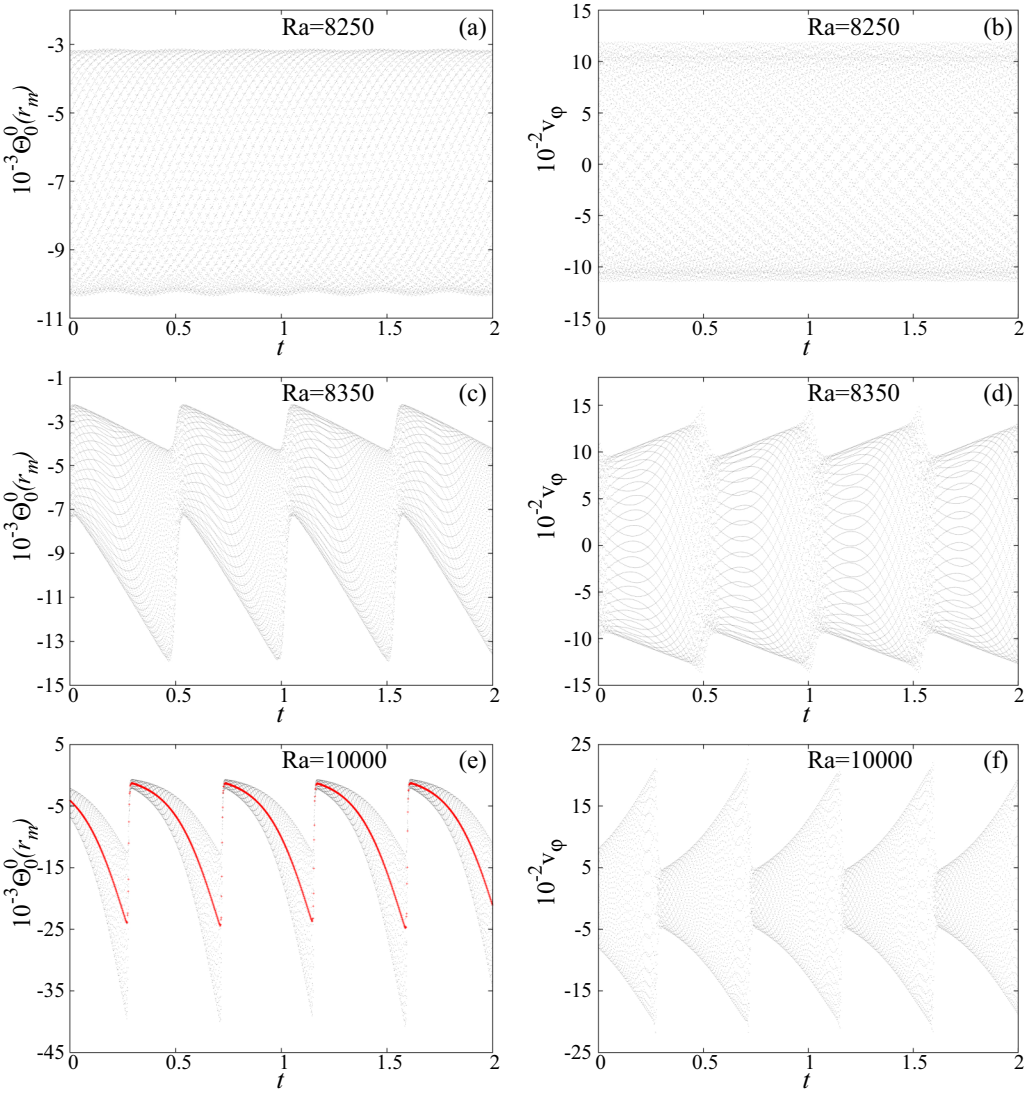

FIG. 12. (a, c, e) Temporal evolution of the coefficient of the perturbation of the temperature $\Theta_0^0(r_m)$, and (b, d, f) of the azimuthal component of the velocity field $v_\varphi(r_o, \pi/3, \varphi)$. In panel (e) the thick curve (red online) corresponds to the Poincaré sections taken at $\Phi_1^0(r_m) = 0$. The parameters are $E = 10^{-4}$, $Pr = 10^{-3}$.

by the two periodic orbits. It is the unstable manifold of the inner, i.e, the orbits starting close to the cycle spiral escaping from it, moving on this surface. They approach the outer unstable cycle because the annulus is also part of the stable manifold of the second periodic orbit. This first stage corresponds to the increase of the amplitude of the oscillations of Figs. 12(e) and 12(f).

Another cleaner projection of the annular manifold is shown in Fig. 13(c), which contains also the unstable periodic orbit at the same value of the parameters but on the main branch of Fig. 1 (large closed curve in black online). It does not match any of the two before mentioned. Therefore they are probably on branches bifurcated from the main one, or on secondary branches arising from the conduction state, which are unstable from the very beginning and have not been computed.

The trajectory that approached the second cycle is then repelled along its unstable manifold, moving out of the annular surface, and being sent back quickly to the first periodic orbit, nearly

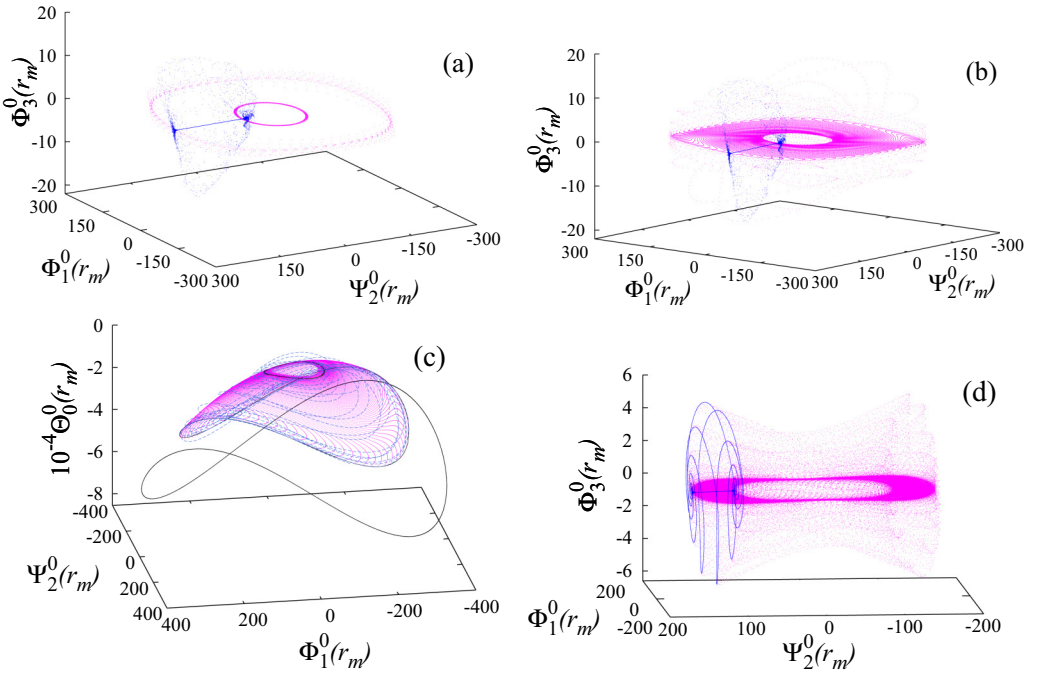

FIG. 13. (a, b) Surface corresponding to the unstable manifold of a cycle and contained in the stable manifold of another, at Ra = 10 000 (in magenta online), and the Poincaré section cutting the $\Phi_1^0(r_m) = 0$ hyperplane (in blue online). (c) Same surface shown with a different variable in the z axis, including the unstable periodic orbit of the main branch. (d) Same representation as in panel (b) for the resonant three-torus at Ra = 8400. The other parameters are $E = 10^{-4}$, $Pr = 10^{-3}$.

completing what it is called a heteroclinic cycle, of either three fundamental frequencies or temporally chaotic [see dots outside the horizontal surface of Fig. 13(b) and dashed line of Fig. 13(c), blue online]. This second stage coincides with the fast decrease of the amplitude of the oscillations. The points that accumulate on a line of the Poincaré section lie on the connecting annular manifold, and the cloud of points of Figs. 13(a)–13(b) (blue online) and the vertical lines of Fig. 12(e) (red online) represent the collapse following the inverse path.

Figure 13(d) shows the same plot as Fig. 13(b) for a resonant three-torus. In this case, instead of filling a 3D volume the trajectories (shown again with dots) are contained on a three-sheet spiral surface.

The mean values of the kinetic energies, and maximum heat flux and helicity for the nonperiodic solutions are included in Figs. 2(b), 3(b), and 4(b). They were calculated as before, and for the solution of doubled period, $t = 2/f_3$ was taken as final integration time. As for the torsional periodic orbits, the components of the energy $\overline{K}_T$ and $\overline{K}_P$ are almost equal and constant, and nearly keep the value reached at the Neimark-Sacker bifurcation. Only the quasiperiodic orbits have a slightly higher $\overline{K}_T$ [full circles in Fig. 2(b)]. The parts $\overline{K}_s$ and $\overline{K}_a$ are shown in Fig. 3(b). The former remains negligible in front of the latter, which almost keeps the value attained at the bifurcation point. In contrast, the maximum values of Nu and H reflect very well the different dynamics found by increasing Ra. The quasiperiodic orbits maintain the values achieved for the stable periodic orbits. With the appearance of a third frequency there is a growth of both quantities with a slope similar to that of the periodic orbits, and from Ra $\approx$ 8500, when the flow becomes chaotic, the slope decreases.

The asymptotic theory of Zhang *et al.* [18] assumes that torsional convection is dominated at first order by inertial oscillations, which do not generate mean flow, while buoyancy forces appear only at next order to overcome the viscous dissipation. Then the torsional solutions are in fact perturbations

of inertial modes. On the other hand, the theory of Herreman and Lesaffre [32] predicts that simple inertial waves cannot drive dynamos at leading order; however, the asymmetry of the solutions giving rise to a ratio K_a/K_s larger than one was related in Ref. [20] to the generation of hemispherical dynamos. Then the large helicity, the high amplitude of the modulated fluctuations, with periodic slow rising and subsequent rapid and irregular decay for $\mathrm{E} = 10^{-4}$, and the large K_a/K_s, observed at high Ra, make the 2D torsional nonperiodic oscillations possible candidates for generating magnetic fields.

The behavior of the velocity field and the temperature during the regular oscillations that increase their amplitude resembles very much that described in Sec. III. When the amplitude of the oscillations quickly falls, there is an irregular interchange of the sign of the temperature between the north and south hemisphere but following a similar pattern. The low-amplitude oscillations also follow the regular interchange, but the fields are much weaker. The same holds for the vertical alternating movement of the hot core, which almost vanishes after the fast transient.

V. CLOSING REMARKS

Axisymmetric torsional solutions of convection in rotating fluid spheres have been studied. Although the Ekman numbers considered here are far from those of the planetary interiors and stars, it is possible to guess some properties of these flows at lower E from the comparison of the two pairs of parameters used in this paper. For any E one should expect inertial chaotic torsional oscillations of basic short period of order E, i.e., of the order of the period of rotation, $2\pi\,\mathrm{E}$. Moreover, since the secondary bifurcation is closer to the first as E decreases, high-amplitude nonperiodic oscillations would be found from the beginning of convection. On the other hand, since the torsional orbits of complex time dependence are very inefficient for convective heat transport at any time instant, and, in addition, the corresponding flux across the outer sphere decreases with decreasing E (see Fig. 4), they seem unable to release much more heat from the interiors of the celestial bodies than by conduction and/or radiation. However, the hot core of the fluid sphere is markedly perturbed due to its axial oscillation, as can be seen in animation 3 [30]. The kinetic energy is concentrated in the surface of the sphere, and it propagates latitudinally in agreement with Ref. [19].

The Hopf bifurcation leading to torsional periodic orbits is supercritical for both sets of parameters studied, i.e., when $\mathrm{Pr}/\mathrm{E} = O(10)$. This result is in agreement with those of Refs. [29,33]. Their authors found, from a quasigeostrophic approximation for the velocity and a fully 3D temperature field in Ref. [29] and from 3D simulations in Ref. [33], both at very low E and Prandtl numbers of the order of those used here, that for liquid metals the onset of convection can be sub- or supercritical depending on E. Moreover, Kaplan *et al.* conclude that for Péclet numbers $\mathrm{Pe} \gtrsim 10$ the Reynolds stresses are able to sustain subcritical convection, and they estimated that this effect is stronger at planetary core conditions, i.e., when $\mathrm{Pr}/\mathrm{E} = O(10^{10})$. In the present case, taking as characteristic velocity the maximum value over the full sphere [$U = O(10^2)$], Pe remains always below 10.

Although the nonlinear terms of the Navier-Stokes equations enforce the appearance of the symmetrical components of the velocity field, at low E the time- and volume-averaged kinetic energy of the periodic torsional solutions is mainly antisymmetric, and it splits equally in the poloidal and the toroidal components. The kinetic energy of the quasiperiodic and other complex time-dependent solutions has the same characteristics and almost maintains a constant value from the Neimark-Sacker bifurcation. However, the amplitude of the oscillations increases quickly with Ra.

Since the periodic solutions are symmetric cycles and the quasiperiodic orbits preserve this symmetry globally, the third Hopf bifurcation can give rise to stable solutions to axisymmetric perturbations with three independent frequencies instead of temporal chaos. At $\mathrm{E} = 10^{-3}$ the transition to temporal chaos follows a classical local route, and after the appearance of the third frequency, a new bifurcation leads to chaos. It is like a Ruelle-Takens via, but affected by the symmetries. However, at $\mathrm{E} = 10^{-4}$ the transition takes place via a global dynamics. Quasiperiodic orbits which seem to be close to heteroclinic cycles connecting two unstable periodic orbits have

been found before chaos arises. Time evolutions with initial conditions taken on the unstable part of the main branch of periodic orbits evolve towards the complex time-dependent solutions described above. The quasiperiodic solutions are very robust and can be observed for a large range of Ra.

ACKNOWLEDGMENTS

This research has been partially supported by the Spanish Ministry of Economy and Competitiveness and European Regional Development Fund, under grant MINECO/FEDER FIS2016-76525-P, and by the Catalan Agència de Gestió d'Ajuts Universitaris i de Recerca under grant 2017-SGR-1374.

APPENDIX: IMPLEMENTATION OF THE CONSERVATION OF THE ANGULAR MOMENTUM

To ensure that $dL_z(t)/dt = 0$ during the integration the following strategy was adopted. From Eq. (7) it turns out that

$$\frac{dL_z(t)}{dt} = 2\sqrt{6}\pi \int_0^{r_o} r^3 \partial_t \Psi_1^0(t, r)\, dr.$$

Moreover, if $\Psi_1^0(t, r) = r$ and the rest of spherical harmonic coefficients of Ψ are zero, then the vector field $\boldsymbol{v} = \boldsymbol{\nabla} \times (\Psi \boldsymbol{r})$ is a solid-body rotation about the vertical axis. After computing the vector field of Eq. (5) we modify $\partial_t \Psi_1^0(t, r)$ by subtracting the function Kr such that

$$\int_0^{r_o} r^3 \left(\partial_t \Psi_1^0(t, r) - Kr\right) dr = 0.$$

This gives

$$K = \frac{5}{r_o^5} \int_0^{r_o} r^3 \partial_t \Psi_1^0(t, r)\, dr.$$

This means adding a body force proportional to a solid-body rotation velocity field. The function Kr satisfies the same boundary conditions as $\Psi_1^0(t, r)$ and $\partial_t \Psi_1^0(t, r)$. The integral is approximated by a quadrature formula on the same set of Gauss-Lobatto points used in the radial direction [34]. If w_i are the weights, then

$$\int_0^{r_o} r^3 \partial_t \Psi_1^0(t, r)\, dr \approx \sum_{i=0}^{N} w_i r_i^3 \partial_t \Psi_1^0(t, r_i).$$

Since the term added to the vector field is linear in Ψ_1^0, exactly the same correction must be added into the first variational equations when they are needed during the Krylov iterations for the computation of the periodic orbits.

[1] J. R. Lister and B. A. Buffet, The strength and efficiency of thermal and compositional convection in the Earth's core, Phys. Earth Planet. Inter. **91**, 17 (1995).

[2] M. Net, F. Garcia, and J. Sánchez, Numerical study of the onset of thermosolutal convection in rotating spherical shells, Phys. Fluids **24**, 064101 (2012).

[3] K. Zhang and X. Liao, On inertial waves and oscillations in a rapidly rotating fluid spheroid, J. Fluid Mech. **504**, 1 (2004).

[4] M. Le Bars, Flows driven by libration, precession, and tides in planetary cores, Phys. Rev. Fluids **1**, 060505 (2016).

[5] P. H. Roberts, On the thermal instability of a rotating fluid sphere containing heat sources, Phil. Trans. R. Soc. Lond. A **263**, 93 (1968).

[6] F. H. Busse, Thermal instabilities in rapidly rotating systems, J. Fluid Mech. **44**, 441 (1970).
[7] C. R. Carrigan and F. H. Busse, An experimental and theoretical investigation of the onset of convection in rotating spherical shells, J. Fluid Mech. **126**, 287 (1983).
[8] J. I. Yano, Asymptotic theory of thermal convection in a rapidly rotating system, J. Fluid Mech. **243**, 103 (1992).
[9] K. Zhang, Spiralling columnar convection in rapidly rotating spherical fluid shells, J. Fluid Mech. **236**, 535 (1992).
[10] C. A. Jones, A. M. Soward, and A. I. Mussa, The onset of thermal convection in a rapidly rotating sphere, J. Fluid Mech. **405**, 157 (2000).
[11] F. H. Busse, Convective flows in rapidly rotating spheres and their dynamo action, Phys. Fluids **14**, 1301 (2002).
[12] E. Dormy, A. M. Soward, C. A. Jones, D. Jault, and P. Cardin, The onset of thermal convection in rotating spherical shells, J. Fluid Mech. **501**, 43 (2004).
[13] F. M. Al-Shamali, M. H. Heimpel, and J. M. Aurnou, Varying the spherical shell geometry in rotating thermal convection, Geophys. Astrophys. Fluid Dyn. **98**, 153 (2004).
[14] M. Net, F. Garcia, and J. Sánchez, On the onset of low-Prandtl-number convection in rotating spherical shells: Non-slip boundary conditions, J. Fluid Mech. **601**, 317 (2008).
[15] A. P. Bassom, A. M. Soward, and S. V. Starchenko, The onset of strongly localized thermal convection in rotating spherical shells, J. Fluid Mech. **689**, 376 (2011).
[16] F. Garcia, J. Sánchez, and M. Net, Antisymmetric Polar Modes of Thermal Convection in Rotating Spherical Fluid Shells at High Taylor Numbers, Phys. Rev. Lett. **101**, 194501 (2008).
[17] J. Sánchez, F. Garcia, and M. Net, Critical torsional modes of convection in rotating fluid spheres at high Taylor numbers, J. Fluid Mech. **791**, R1 (2016).
[18] K. Zhang, K. Lam, and D. Kong, Asymptotic theory for torsional convection in rotating fluid spheres, J. Fluid Mech. **813**, R2 (2017).
[19] D. Kong, K. Zhang, K. Lam, and A. P. Willis, Axially symmetric and latitudinally propagating nonlinear patterns in rotating spherical convection, Phys. Rev. E **98**, 031101(R) (2018).
[20] M. Landeau and J. Aubert, Equatorially asymmetric convection inducing a hemispherical magnetic field in rotating spheres and implications for the past Martian dynamo, Phys. Earth Planet. Inter. **185**, 61 (2011).
[21] J. Sánchez, F. Garcia, and M. Net, Computation of azimuthal waves and their stability in thermal convection in rotating spherical shells with application to the study of a double-Hopf bifurcation, Phys. Rev. E **87**, 033014 (2013).
[22] J. Sánchez, M. Net, B. García-Archilla, and C. Simó, Newton-Krylov continuation of periodic orbits for Navier-Stokes flows, J. Comput. Phys. **201**, 13 (2004).
[23] J. Sánchez, M. Net, B. García-Archilla, and C. Simó, Continuation of periodic orbits in large-scale dissipative systems, in *Proceedings of the Equadiff-2003 Conference*, edited by F. Dumortier, H. Broer, J. Mawhin, A. Vanderbauwhede, and S. Verduyn Lunel (World Scientific, Singapore, 2005), pp. 625–630.
[24] J. Sánchez and M. Net, Numerical continuation methods for large-scale dissipative dynamical systems, Eur. Phys. J. Spec. Top. **225**, 2465 (2016).
[25] J. Sánchez, F. Garcia, and M. Net, Radial collocation methods for the onset of convection in rotating spheres, J. Comput. Phys. **308**, 273 (2016).
[26] P. W. Livermore, C. A. Jones, and S. J. Worland, Spectral radial basis functions for full sphere computations, J. Comput. Phys. **227**, 1209 (2007).
[27] A. C. Hindmarsh, ODEPACK, A systematized collection of ODE solvers, in *Scientific Computing*, edited by R. S. Stepleman *et al.*, IMACS Transactions on Scientific Computation (North-Holland, Amsterdam, 1983), Vol. 1, pp. 55–64.
[28] F. Garcia, M. Net, B. García-Archilla, and J. Sánchez, A comparison of high-order time integrators for the Boussinesq Navier-Stokes equations in rotating spherical shells, J. Comput. Phys. **229**, 7997 (2010).
[29] C. Guervilly and P. Cardin, Subcritical convection of liquid metals in a rotating sphere using a quasi-geostrophic model, J. Fluid Mech. **808**, 61 (2016).

[30] See Supplemental Material at http://link.aps.org/supplemental/10.1103/PhysRevFluids.4.013501 for three animations of the evolution of Θ, the full temperature, and the kinetic energy.
[31] Y. A. Kuznetsov, *Elements of Applied Bifurcation Theory* (Springer, Berlin, 1998).
[32] W. Herreman and P. Lesaffre, Stokes drift dynamos, J. Fluid Mech. **679**, 32 (2011).
[33] E. J. Kaplan, N. Schaeffer, J. Vidal, and P. Cardin, Subcritical Thermal Convection of Liquid Metals in a Rapidly Rotating Sphere, Phys. Rev. Lett. **119**, 094501 (2017).
[34] C. W. Clenshaw and A. R. Curtis, A method for numerical integration on a automatic computer, Numer. Math. **2**, 197 (1960).